

Radar reflections from sedimentary structures in the vadose zone

**Remke L. Van Dam^{1,4‡}, Elmer H. Van Den Berg¹, Marcel G. Schaap²,
Lucas H. Broekema³ & Wolfgang Schlager¹**

¹Faculty of Earth Sciences, Vrije Universiteit, De Boelelaan 1085, 1081 HV Amsterdam, The Netherlands

²George E. Brown Jr. Salinity Laboratory, 450 Big Springs Road, Riverside, CA 92507-4617, USA

³ESRI Nederland, Stationsplein 45, 3001 GA Rotterdam, The Netherlands

⁴Current address: Bemuurde Weerd o.z. 7, 3514 AN Utrecht, The Netherlands

‡corresponding author; e-mail: rvd@geopuls.nl

Abstract

Ground-penetrating radar (GPR) is considered a suitable technique to image sedimentary structures in the vadose zone because small texture variations lead to changes in capillary pressure and water content that, in turn, cause reflection of electromagnetic waves. To study exactly how GPR reflections are generated by sedimentary structures, GPR profiles of an eolian sedimentary succession are combined with measurements of textural, electromagnetic, and water-retention characteristics from a trench. Time-domain reflectometry indicates that small texture variations in the high-angle dune sediment are associated with changes in water content. Synthetics show that these changes cause clear GPR reflections. In an experimental approach to estimate the radar response of structures below the wave resolution, variations in grain-size distribution and porosity in a thin section were used to reconstruct water-retention curves and impedance models of the thinly layered sediment. Synthetic radar records calculated from the impedance models show that reflections from the studied sub-centimeter-scale structures are composites of interfering signals. Although low-amplitude interfering signals will commonly be overprinted by more prominent reflections, they may cause reflection patterns that change with frequency and do not represent primary bedding.

1 Introduction

Ground-penetrating radar (GPR) is frequently used to image sedimentary structures for reconstruction of depositional history or for reservoir characterization. It is generally understood that changes in texture cause variations of water content (e.g., Mishra et al., 1989; Hänninen, 1992). Because water has dielectric properties that are highly contrasting with those of air and quartz, the water content of sediment governs the behavior of radar waves. Thus, water-content variations that are caused by texture variation in sedimentary structures lead to changes in dielectric properties. As radar signals reflect from boundaries between layers with different electromagnetic properties, GPR can be used to image sedimentary structures (e.g., Huggenberger et al., 1994; Kowalsky et al., 2001).

Studies that try to quantify the relationship between textural properties, water content and electromagnetic wave propagation usually consider a large range of grain and pore sizes (e.g., Hubbard et al., 1997; Endres, 2000). Frequently used regression functions (Gupta and Larson, 1979; Saxton et al., 1986) and the more sophisticated physico-empirical model of Arya and Paris (1981) relate water content to bulk density and to percentages of sand, silt, clay and organic matter. Knoll and Knight (1994) presented a dielectric mixing model that includes clay-volume fraction. Sutinen (1992) quantified relations between grain size, water content, and dielectric properties. He found that the percentage of clay and silt had a large effect on the dielectric properties but observed no correlation between dielectric properties and the grain size of sand and gravel.

Eolian sediment, discussed in the present study, commonly has a very narrow range of grain sizes and usually contains only grains in the sand fraction. Still, eolian deposits produce clear GPR reflections (e.g., Bristow et al., 2000). For these rather uniform sedimentary facies, important questions about reflection of radar signals remain unsolved. With respect to GPR, it is not known in great detail which textural characteristics (e.g., grain size, sorting, packing, grain shape, porosity) control the actual reflection. Also, the minimum required variation in these textural characteristics to generate a reflection is unclear. Furthermore, little is known about the contribution of reflection and signal interference from layering smaller than the vertical resolution limit, commonly assumed to be a quarter wavelength, $\lambda/4$ (e.g., Huggenberger, 1993). Typical values for $\lambda/4$ in moist sand ($v = 0.12 \text{ m ns}^{-1}$) range from 0.3 to 0.033 m for 100- to 900-MHz frequencies, respectively.

Interference of radar reflections from small-scale electromagnetic-property variation in geologic material and sediment is very common (e.g., Clement et al., 1997) but has never been studied in detail. Few modeling studies on this issue have been performed. In seismic reflection this problem has gained much more attention from both fields of interpretation (e.g., Roksandic, 1995) and modeling (e.g., Kallweit and Wood, 1982). Gochioco (1992) shows that layers as thin as one-fortieth the width of the dominant wavelength are detected. However, thin sediment lay-

ers are commonly not isolated and are often more narrowly spaced than vertical resolution, such that recorded reflections are composites of several interfering signals (e.g., Mayer, 1980; Knapp, 1990; Bracco Gartner, 2000). As a result, the seismic response from thinly layered sediment may not represent distinct geologic horizons (Mayer, 1979).

To address the above questions, we selected a study area in eolian dune deposits near the Dutch coast, south of Katwijk aan Zee (Figure 1). The deposits consist of units with clean wind-blown quartz sand, separated by soils (Van Dam et al., accepted2). The upper unit, characterized by high-angle cross-stratification, was used for this study. The site was surveyed using a grid of GPR lines. Next, trenches were dug that allowed us to study and sample the sediment and to measure electromagnetic properties. Lacquer peels were collected for macroscopic study of sedimentary structures and samples for grain-size analyses were taken from a vertical transect. Also, core plugs were collected to determine water-retention characteristics of the sediment in the laboratory. Time-domain reflectometry (TDR) was used to obtain direct and detailed information on the electromagnetic properties of the sedimentary structures. Finally, box cores were collected for microscopic texture analysis in thin sections. The small-scale textural information from the digitized thin sections was used to estimate water retention and dielectric properties perpendicular to the sedimentary bedding. The TDR measurements and thin sections were used to construct models of electromagnetic wave impedance and to calculate synthetic radar traces. The TDR-based synthetic radar traces were used to study signal interference. The thin-section based model serves as a more theoretical approach to improve understanding of propagation and reflection of GPR waves within and across sedimentary structures.

2 Water retention

The primary reason that GPR can image sedimentary structures is that the water content of unsaturated sediments is a function of sediment properties that vary most prominently perpendicular to depositional layering. Porous media in natural unsaturated conditions retain some water, which indicates that forces prevent part of the interstitial moisture from draining. These so-

called matric forces can be subdivided into adsorption and capillary forces (De Marsily, 1986). Adsorption is the strong molecular attraction between water and solids that creates a thin water film around sediment particles. The amount of adsorbed water depends on the specific-surface area of the solid phase. Because adsorbed water has a low relative permittivity (Roth et al., 1990; Saarenketo, 1998) and because the specific-surface area of sand is small (Sutinen, 1992), its influence on electromagnetic waves is limited. Capillary forces result from pressure differences between water and air phases in the pores and control the amount of free water in the pore space. The capillary pressure is inversely proportional to the pore radius (r). Matric forces thus exert suction on the pore water, usually expressed by the pressure head (h) or suction potential (pF), where $pF = \log |h|$. The term 'field capacity' is defined as the specific suction potential when drainage under the influence of gravity has ceased. The natural unsaturated conditions referred to in this paper are field-capacity conditions at pF 2.

The relation between suction potential and volumetric water content (θ) is a fundamental soil hydrological property (Arya and Paris, 1981) that is related to the size distribution and connectivity of the pores (Vogel and Roth, 1998; Fens, 2000). Pore bodies with wide entry channels (pore throats) will drain at low suction, whereas those with narrow channels drain at higher suction (Bouma, 1977). It is generally accepted that, at field-capacity conditions and for equal porosity values, fine-grained sediment with small pores has a higher θ than coarse-grained sediment. The same holds for poorly sorted sediment relative to well-sorted sediment. Simple laboratory experiments allow measurement of the θ - pF relation. In the experiments, initially saturated sediment cores are drained and water content is measured at specific suction potentials. Water-retention curves can be modeled by fitting the measured θ - pF pairs with Van Genuchten (1980):

$$\theta = \theta_r + \frac{\theta_s - \theta_r}{(1 + (\alpha_{vg}|h|)^n)^{m_{vg}}}. \quad (1)$$

Here, θ_r and θ_s represent the residual and saturated water contents, respectively, α_{vg} [cm^{-1}] and n are parameters to fit the shape and position of the curves, and $m_{vg} = 1 - n^{-1}$. This experimental method is time consuming and cannot account for small-scale texture variations

related to sedimentary structures that are present in the sample volumes.

Formulas that describe the relation between pore-size distribution and capillary forces also allow calculation of the θ - pF relation. However, the pore-size distribution is difficult to measure and, consequently, methods like network modeling (Vogel, 2000) and percolation theory are based on simplified assumptions for pore structure. The good correlation between pore-size distribution and grain-size distribution (GSD) of eolian sediment (Van Den Berg et al., in review), allows the use of GSD as a proxy for water retention in non-saturated sediment (Mishra et al., 1989). Next to GSD, total porosity (η) is a factor of importance for the water retention in sediment as it is generally a measure for the packing. Assuming sediment with equal grain-size distribution, tighter packing results in smaller pores that hold capillary water with greater ease. Neural network models allow calculation of the θ - pF relation of sediment using its GSD and η (Schaap and Bouten, 1996).

3 Test site

3.1 Experimental procedure

The 11 × 16-m test site was surveyed with a grid of 2-D GPR lines (Figure 1), using a pulseEKKO radar system with 25-, 100-, 225-, 450-, and 900-MHz antennas. 450- and 900-MHz antennas were used to image a small, 3 × 4-m area along the long axis of the grid in greater detail (Table 1). Subsequent to the GPR measurements, 2 trenches (A and I), each 3-m deep, were dug for detailed study and sampling of the sediment. Lacquer peels were made for macroscopic study of textural characteristics. A few core plugs were collected for laboratory measurements of water retention (Figure 2). The core plugs with a volume of 45 cm³ were sampled by pushing a metal ring into the sediment. The metal rings have walls of minimum thickness, so as to reduce sediment disturbance. Along vertical sections in the wall of trench I, TDR was used to obtain detailed information on dielectric properties in the subsurface, and samples were collected for macroscopic analysis of textural properties (Table 2). Although the TDR and GPR measurements are separated by a one-week time interval we expect no large

ambiguities as we removed the wind-dried surface of the trench before measuring TDR data.

To obtain detailed information on the variation in textural characteristics and electromagnetic properties normal to the high-angle sedimentary bedding, we selected three sites I21, I22, and I23 in the detailed study area in trench I (Figure 2b). Both I21 and I22 were set at the location of known fine-grained foreset tops; I23 was set at a position where no foreset was visible. To measure variation in electromagnetic wave velocity perpendicular to the bedding we measured 4 detailed TDR sections with a 0.02-m spacing at these locations (Figure 2b).

In an experimental approach to measure small-scale variations in textural characteristics and electromagnetic properties, we collected three $0.05 \times 0.08 \times 0.15$ -m (height \times width \times length) undisturbed box cores at sites I21, I22, and I23 (Figure 2b). The box cores have thin metal walls, so as to reduce sediment disturbance. In the laboratory, the box cores were impregnated with a blue epoxy-resin dye and thin sections were prepared perpendicular to the sedimentary bedding to reveal the maximum textural variation. Next, the thin sections were used for image analysis of the sediment characteristics and reconstruction of water-retention curves. Direct correlation between the box-core results and TDR measurements is difficult because the box cores were collected a few centimeters deeper into the quarry wall to avoid sediment disturbance caused by the TDR pins. Also, before impregnation with epoxy resin about one-third of the box cores was used to sample core plugs for measurement of water retention (Figure 2b).

3.2 Sedimentology and stratigraphy

The sediment at the test site is subdivided into 7 units. Units 1, 3, 5, and 7 consist of clean windblown sands, whereas units 2, 4, and 6 are soils (Figure 2a). The ages of sampled organic material show that unit 6 was formed between 1260 and 1425 AD (Van Dam, 2001). The sediment below unit 6 was deposited as the relatively low Older Dunes that formed on top of a prograding coastal barrier system (Jelgersma et al., 1970). After about 1200 AD, a period of coastal erosion marked the onset of the formation of the so-called Younger Dunes. Increased sediment supply led to the development of dunes that were up to 35-m high.

Unit 7 in trench I, on which the present study focuses, is characterized by high-angle cross-

stratification, dipping at a maximum angle of 40° towards the southeast. We attribute the absence of a sharp crest to a relatively rapid filling of the depression in which unit 6 was formed. The lacquer peels show two 0.2 to 0.3-m thick convex-upward foresets in unit 7 (Figure 2b). They are characterized by a top layer (around 5-cm thick) with slightly finer grain size than the bulk sediment. Also, sub-centimeter-scale lamination is present within the high-angle foresets. The photographs of the lacquer peels do not have enough detail and contrast to show this lamination. The average grain size of the studied sediment in unit 7 is around $280 \mu\text{m}$ (medium sand). The average silt and clay content is 0.6% and 0.4%, respectively (Table 2).

3.3 GPR measurements

Fundamental properties that control the behavior of GPR signals are dielectric permittivity (ϵ), electrical conductivity (σ), and magnetic permeability (μ), which together define electromagnetic wave impedance (Z). Impedance contrasts in the subsurface cause part of the propagating electromagnetic energy, proportional to the magnitude of change, to be reflected. For most natural sediments, variations in μ are insignificant (e.g., Daniels et al., 1988; Van Dam et al., accepted1). In low-loss material such as clean, dry sand, the influence of σ on the electromagnetic signal is negligible at GPR frequencies (Davis and Annan, 1989). In contrast, ϵ plays an important role in both propagation and reflection of electromagnetic waves. If one defines relative permittivity $\epsilon_r = \epsilon/\epsilon_0$, where ϵ_0 is the permittivity of free space, ϵ_r of water is around 80, whereas air and quartz have values of 1 and around 4, respectively. Thus, water content governs the relative permittivity and electromagnetic wave impedance of sediment. The electromagnetic wave velocity (v) is found by $v = c_0/\sqrt{\epsilon_r}$, where c_0 is the velocity in vacuum ($3 \times 10^8 \text{ m s}^{-1}$). Radar-wave reflectivity can be found from the difference in electromagnetic wave impedance at layer transitions and can be simplified with $RC = (\sqrt{\epsilon_{r2}} - \sqrt{\epsilon_{r1}})/(\sqrt{\epsilon_{r2}} + \sqrt{\epsilon_{r1}})$, where ϵ_{r1} and ϵ_{r2} are relative permittivity above and below the transition, respectively. The quality and sharpness of the reflection depends on the transition-zone width (vertical range over which ϵ_r changes), relative to the predominant wavelength (W/λ). A sharp transition in ϵ_r with depth gives a sharp reflection. In contrast, a gradual change in ϵ_r causes signal dispersion. An-

nan et al. (1991) estimate that $W/\lambda < 0.3$ gives a sharp reflection. Under natural unsaturated conditions the transition-zone width depends on the total difference in water content above and below the contrast as well as on the water-retention characteristics of the sediment above the contrast (Young and Sun, 1999).

Using common-mid-point measurements (Figure 1) the velocity for unit 7 was estimated around 0.12 m ns^{-1} , which allowed for an accurate time-to-depth conversion. The 450-MHz GPR profile shows several continuous sub-horizontal reflections (① and ②, Figure 3a), which result from the soil horizons (Figure 2). Between meters 6 and 15 the upper 0.75 m shows dipping reflections. These reflections result from the high-angle cross-stratified dunes in unit 7 (Figure 2). The 900-MHz GPR profile images several high-angle foresets in greater detail (③ and ④, Figure 3b). Next to the reflections of the high-angle stratification, the 900-MHz image shows some short sub-horizontal reflections (right of ③ in Figure 3b). These reflections are low amplitude and cannot be linked to sedimentary structures in the lacquer peels. They possibly originate in a feature at the surface positioned around meter 6.6. The reflection from the top of the soil horizon below unit 7 is rather vague. This is partly caused by the large width of the transition zone, W . For a transition zone of 0.1 m, as observed at the boundary between unit 7 and unit 6 (Van Dam et al., accepted2), and a velocity of 0.12 m ns^{-1} , W/λ is 0.75 for the 900-MHz signal. Consequently, the signal experiences dispersion and a decrease in reflection amplitude.

4 TDR measurements

Time-domain reflectometry was developed to characterize the conductivity and water content of soils through measurement of their electromagnetic properties. The method is based on the propagation of an electromagnetic signal along a probe that is inserted into the sediment (e.g., Heimovaara and Bouten, 1990). Next to measurements of temporal changes, one can use TDR to construct vertical profiles of electromagnetic properties (Topp and Davis, 1985; Van Dam and Schlager, 2000). The relative permittivity (ϵ_r) can be calculated from the travel time of the

signal in the sediment. The volumetric water content (θ) can be found by substitution of ϵ_r in empirical equations (e.g., Topp et al., 1980).

Vertical TDR sections show that the relative permittivity (ϵ_r) in unit 7 varies between 3.75 and 4.75 (Figure 4a,b), which is around the typical value of 4 for dry sand. The grain size is relatively small at the top and bottom of the measured section, and larger in the middle part (Figure 4c). Smaller grain sizes lead to a higher amount of capillary water to be present in the sediment. The two finer-grained foreset tops that are present in the lacquer peels can be identified on the TDR sections by a local increase in ϵ_r and are marked by labels ③ and ④ (Figure 4a,b). They correspond approximately with the numbered clinofolds in Figure 3 and foreset tops in Figure 2. Events ③ and ④ are two of several similar but unexplained permittivity excursions in the TDR sections (Figure 4), that may be related to the sub-centimeter-scale lamination observed in the lacquer peels.

To obtain detailed information on the variation in electromagnetic properties perpendicular to the foresets, TDR measurements with a 0.02-m spacing were conducted at the three sites I21, I22, and I23. Three of the detailed sections were set at locations of known foreset tops; the fourth section was taken at a position where no foreset was visible (Figure 2b). The TDR measurements at foreset locations show a small but distinct increase in ϵ_r from around 3.75 to values between 4.25 and 4.75 (Figure 5). The increase marks the transition to the fine-grained foreset top. The finer grain sizes of the foreset tops cause an increase in capillary water. The lower end of the 5-cm thick foreset tops is marked by a decrease in ϵ_r . The transition-zone width (W) of increase and decrease in ϵ_r is around 0.04 m. W/λ for a 900-MHz GPR wave would be around 0.3, which is just at the transition between a sharp radar reflection and significant dispersion (Annan et al., 1991). The TDR measurements were used to construct models of electromagnetic wave impedance that allow synthetic modeling of GPR reflections for the foresets. Results of this will be discussed later, along with the impedance models of the thin sections.

5 Analysis of thin sections

5.1 Image analysis

The primary objective of image analysis of thin sections in this study is to estimate variations in water content and electromagnetic properties from textural characteristics on a finer scale than TDR can measure. Here, the thin section from box core I21 is described (Figure 2b). As previously mentioned, the positional constraint of the thin section image relative to the foreset top is not very strong. Therefore, comparison of the thin-section measurements and TDR section 1223.005 is difficult. Four high-resolution (176×176 pixels per mm^2) digital photographs were taken with some overlap (covering an area of approximately 65×15 mm) in a transect along the long axis of the thin section. We corrected for small spectral inhomogeneities between photographs using histogram matching in image processing software ERDAS IMAGINE. Also, we used the software for maximum-likelihood classification to obtain binary images of solid grains and pores. To prevent edge effects on the margins, the images were cropped. To obtain unbiased measures for textural parameters from the binary images we separated touching grains using a cutting procedure by Van Den Berg et al. (in press). These processing steps were performed on the thin section images to get the final image that was used for the actual measurements (Figure 6).

The final image was analyzed for a series of textural characteristics, including grain-size distribution (GSD) and porosity (η), using the method described in Van Den Berg et al. (in review). With most textural variation present in the direction perpendicular to the sedimentary layering we used a rectangular measurement window to estimate the textural characteristics in the thin section (Figure 6). We assume textural variation parallel to the bedding (the long axis of the measurement window) to be constant. The measurement window had a height of 1.5 mm and was moved with increments half the height of the window to obtain 85 samples (Figure 6).

The measured 2-D grain size was converted to 3 dimensions by applying a multiplication factor of $4/\pi$, which is strictly spoken only valid for spheres. We accepted the assumption as a reasonable simplification. The mean grain size shows a variation between 200 and 325 μm

(Figure 7a), which is comparable to the variation that was found using laser particle-size measurements (Figure 4c). The variation in mean grain size shows a coarsening-downward trend from sample 85 to 20 and a subsequent and sudden drop in mean grain size below sample 20. The porosity (η) is easily found from the binary image and varies between 0.32 and 0.4 (Figure 7b). Around sample 63 there is a distinct step in η whereas mean grain size varies little. There is also a large step in porosity between samples 20 and 25. Although the zone with a large variation in porosity coincides with a large variation in mean grain size (samples 20-45) there is no correlation between mean grain size and porosity (Figure 8). The transitions in grain size and porosity (Figure 7a,b) are not always as sharp as they appear in the image (Figure 6). This probably is the result of the moving average window and the fact that transitions may not be perfectly perpendicular to the long axis of the image.

5.2 Estimated small-scale water-retention characteristics

To estimate the θ - pF relations from the textural characteristics of the thin section we used a neural network model that was developed for similar sediment as in the present study and required input of cumulative grain-size distribution and porosity. The original data set comprised 204 undisturbed core plugs of 15 sandy forest soils in The Netherlands. The samples were taken between 0 and 1-m depth and contain little clay and organic matter (Schaap and Bouten, 1996). Neural networks are black-box models that are able to learn relations between data without prior model concept (Schaap, 1996), which makes the method very useful for analyzing data sets that lack understanding of all physical relations.

The 85 GSD's that were measured from the thin section were fitted with Haverkamp and Parlange (1986):

$$GSD(d) = \frac{1}{(1 + (d_{gsd}d^{-1})^{n_{gsd}})^p}. \quad (2)$$

Here, $GSD(d)$ is the cumulative weight fraction, d is grain size, d_{gsd} and n_{gsd} are measures of the average grain size and grain-size uniformity, respectively, and $p = 1 - n_{gsd}^{-1}$. The average root-mean-square error of the measured and fitted cumulative grain-size distributions was 0.019. For 4 specific measurements with contrasting mean grain size and porosity (Figure 7a,b), the fitted

grain-size distributions (Figure 9a) illustrate the variation in grain size and sorting. Samples 61 and 69 are fine grained and have a narrow GSD (well sorted). Samples 20 and 27 are coarser grained, with sample 27 being relatively well sorted and sample 20 poorly sorted (Table 3). Also, the samples show a difference in porosity (Figure 7b). Samples 27 and 61 have a low porosity whereas 20 and 69 have a high porosity (Table 3). Although the porosity is somewhat underestimated (Table 3) the fitted GSD's agree well with the measured GSD of core plug I21p (Figure 9a).

Next, the neural network model M6 of Schaap and Bouten (1996) was used to construct water-retention curves for each of the 85 measurements (Table 4). Giving input values for d_{gsd} , n_{gsd} , gravel percentage, organic-matter percentage, and porosity, the neural network generated output values for the Van Genuchten (1980) parameters α_{vg} and n in Equation (1). Curves for the 4 specific measurements illustrate the interplay between porosity and grain-size distribution in the control of water retention (Figure 9b). The porosity determines the saturated water content at zero suction, whereas the grain-size distribution and porosity together determine the inflection point and the steepness and height of the plateau in the curve. Samples 61 and 69 have similar grain sizes but the higher porosity of 69 causes a higher saturated water content. The larger mean pore size (higher porosity) is due to looser packing and leads to a steeper plateau and an inflection point at a lower suction potential. Thus, the sediment at sample 69 drains quicker and its water-retention curve crosses that of sample 61. Samples 20 and 27 have comparable mean grain size but the sediment of sample 20 is poorly sorted and has the widest distribution of grain sizes of all four samples (Figure 9a). This distribution leads to a water-retention curve that is gentler than the others (Figure 9b). Although the sediment for sample 20 starts to drain at the lowest suction values (between pF 0.5 and 1) it drains slowest (see value for n in Table 4).

Comparison of the four specific measurements with the core plug shows that although the plateaus do not exactly match, the overall pattern is very similar (Figure 9b). At pF 2, which is around field-capacity conditions (Van Dam et al., accepted2), the results for the core plug I21p and the neural network results differ by a factor 3. The difference may be caused by the

neural network modeling (the original data set in Schaap and Bouten (1996) contains more silt) or by macro-porosity in the core plug. In modeling GPR reflections, relative contrasts in water content and dielectric properties are more important than the absolute values. We therefore assume the difference around $pF\ 2$ as a reasonable simplification. For all 85 samples, Figure 7c shows the vertical variation in θ at $pF\ 2$, and ranges from around 0.04 to 0.06 (Table 5).

5.3 Dielectric properties

Under the reasonable assumption that the influence of adsorbed water can be ignored, a simple three-phase dielectric mixing model was used to obtain relative permittivity from θ (Bohl and Roth, 1994):

$$\varepsilon_r = (\theta \varepsilon_w^{\alpha_m} + (1 - \eta) \varepsilon_s^{\alpha_m} + (\eta - \theta) \varepsilon_a^{\alpha_m})^{1/\alpha_m}. \quad (3)$$

Here, η is porosity, ε_w is relative permittivity of water, ε_s is relative permittivity of solid material, ε_a is relative permittivity of air, and α_m is a constant (0.5 for isotropic and homogeneous material; Roth et al., 1990). For ε_s we used a value of 3.7 (Van Dam et al. accepted1). The results for the 4 specific samples are given in Table 5. Figure 7d shows that the ε_r values lie between 3.6 and 4.5. Both absolute values and observed range are comparable to those found with the TDR measurements (Figure 4a,b). The most distinct step in permittivity lies between samples 60 and 70 and is associated with variation in porosity. The major step in grain size at sample 20 (Figure 7a) did not result in a prominent permittivity change.

6 GPR synthetic modeling

Using the average of the detailed TDR measurements 1223.005 and 1223.006 (Figure 5) and the ε_r results for the thin section (Figure 7d), we constructed two models of electromagnetic wave impedance. Figure 10 shows the reflection coefficient (RC) based on these impedance models versus depth. The TDR-based model has 0.02-m measurement increments whereas the detailed thin-section model has 0.75-mm measurement intervals. To construct synthetic 1-D GPR traces from the impedance models we used pulseEKKO software (Sensors&Software,

1996). The software transforms the impedance model from a depth scale into a time scale, followed by computation of the impulse response for the layered model. Next, all generated reflections are calculated, including multiples and interlayer reflections. The ground response is obtained by convolution of a standard pulseEKKO wavelet (both 450 and 900 MHz) with the impulse response. One of the assumptions of the software is a vertically incident wave, which we accepted as a reasonable simplification. We ignored losses from spherical-waveform spreading because of the limited thickness of the model. Attenuation was set at a constant value (0.01 dB m^{-1}) because of the limited variation in dielectric properties.

In the reflectivity model for the TDR data (Figure 10a), the first two events at 0.22 and 0.24-m depth are associated with the increase in ϵ_r due to the transition to the fine-grained foreset top (Figure 5). The next two negative events at 0.26 and 0.28-m depth are due to the subsequent increase in grain size and decrease in ϵ_r at the bottom of the around 5-cm thick foreset top. Figure 11 shows the individual contribution of each *RC* event to the composite reflection (stack). In the 900-MHz synthetic trace the first two *RC* events cause clearly visible excursions to the left (Figure 11a). This is an illustration of signal dispersion (indicated by label ① in Figure 10a), and is due to the gradual transition in ϵ_r . The next two events cause reflections with an opposite polarity and partly overlap the two previous reflections (Figure 11a). Here, the overlap causes a large width of the positive excursion in the composite signal between 0.55 and 1.2 ns, relative to the negative excursion between 0 and 0.55 ns. The final two events are too small to recognize in the stacked signal. In the 450-MHz synthetic trace the resolution is too low to distinguish any of the events separately. This image is a stack of 6 different, overlapping waveforms, producing one composite reflection. Figure 11b clearly illustrates that the 450-MHz wavelength is too long to discern both the top and bottom of the around 5-cm thick foreset top ($\lambda/4 \approx 7.5 \text{ cm}$). Here, the first excursions of negative *RC* events 3 and 4 coincide with the second excursions of events 1 and 2, and cause a composite reflection dominated by constructive interference. Accurate comparison of these results with the original GPR images is difficult because of the assumptions in the synthetic modeling. The modeled and original data are different for angle of

wave incidence. Also, losses by attenuation and by spherical-waveform spreading are difficult to accurately model for the part overlying the foreset top. Thus, reflection strengths cannot be compared.

In the detailed thin-section model (Figure 10b), with data points 0.75 mm apart, which is a small fraction of the wavelength (Table 2.1), it is obvious that the vertical resolution of the GPR signal is far too low to resolve the thin lamination. Moreover, radar antennas transmit their energy in a complex three-dimensional pattern (Van Der Kruk, 2001), troubling the attempt to study the radar response of thin lamination using 1-D synthetic models. Nevertheless, from seismic studies we know the importance to stay a few steps ahead of maximum resolution (e.g., Mayer, 1979; Bracco Gartner, 2000) and to understand the behavior of individual wave trains; not only the behavior of the wave form propagating in three dimensions. As is seen in the 900-MHz synthetic trace, individual reflections cannot be distinguished, but groups of events can. The negative RC' s between 0.205 and 0.215 m (indicated by arrow ② in Figure 10b) together form the excursion to the right in the 900-MHz trace. The group of positive RC' s between 0.21 and 0.22 m (indicated by arrow ③ in Figure 10b) cause the stepped pattern in the synthetic trace (indicated by arrow ④ in Figure 10b). Below this the interference by the numerous overlapping waveforms becomes too complicated to distinguish RC events in the synthetic image. The most important indication that the reflected signal is a composite of interfering signals is illustrated by the difference in reflected signal for two different frequencies. The 450-MHz synthetic produces a totally different trace than the 900-MHz one. Also, it becomes apparent from the synthetic models that the reflection pattern in the thin-section synthetics (Figure 10b) has lower mean amplitude than the reflection pattern from the TDR model (Figure 10a). This shows that interference from thinly layered sediment reduces the mean amplitude of radar reflections. Although at the scale of the individual wave train the RC' s in Figure 10b reach those of the TDR-based model, a wavefront propagating in three dimensions will cause a decrease in the amplitude of the interference pattern. In an actual measurement with a 3-D propagating wavefront reflections from changes in permittivity that are thicker and laterally more continuous

will overprint the low-amplitude interfering reflections. Kruse and Jol (submitted) show how thin layers with small impedance contrasts get overprinted by reflections from larger contrasts. However, reflections from sub-centimeter-scale layering may cause loss of energy and may explain, especially in the case of constructive interference and sediment with little along-bedding variation, reflections that do not represent original bedding.

7 Discussion and conclusions

This study began with the premise that although GPR has proven a useful technique for the imaging of sediments, detailed and quantitative knowledge about radar-wave reflection from sedimentary structures is lacking. It is not known in great detail which textural characteristics control water retention and, thus, reflections. Also, the minimum magnitude of change for a reflection is unclear and little is known about the contribution of structures smaller than $\lambda/4$ to the total reflection.

It is shown that water content, and thus GPR reflections in unsaturated sediment, is controlled by the size distribution and connectivity of the pore network. The exact characteristics of the pore network are difficult to estimate. Instead, grain-size distribution and total porosity can be used to estimate water-retention characteristics in sediment. Although other texture parameters such as grain orientation may have an influence on water retention we consider the possible effects to be of minor importance. At field-capacity conditions (around $pF \approx 2$), when GPR is commonly used to study sediment, fine-grained and tightly packed material retains more water than coarse and loosely packed material. The minimum required variation in grain size necessary to produce reflections structures is small. Even the smallest change in water content will cause a contrast in dielectric properties and, thus, reflection of electromagnetic energy. Quantifying the minimum magnitude of change necessary to produce a reflection that is visible in GPR field measurements is less straightforward.

Figure 4c shows a maximum textural variation of $\sim 80 \mu\text{m}$ for unit 7. TDR measurements in this unit show that high-angle GPR reflections of fine-grained foreset tops are caused by ϵ_r

variations between around 3.75 and 4.75. Impedance models based on the TDR measurements across an around 5-cm thick foreset top allowed synthetic modeling of 450- and 900-MHz GPR reflections. The results show that the reflected signal experiences dispersion due to the gradual transition in dielectric properties. The thickness of the foreset top is just around maximum resolution ($\lambda/4$) and reflections from the top and bottom of the foreset top interfere with each other.

The digitized thin-section image rendered detailed information about variation in texture normal to the bedding in an experimental attempt to model the radar response across of sub-centimeter-scale sedimentary layering. A neural network and a dielectric mixing model estimated ϵ_r at field-capacity conditions to vary between 3.6 and 4.5, which agrees well with the values measured with TDR. Models of electromagnetic wave impedance and reflectivity constructed from this 6-cm long transect allowed modeling the GPR response. the GPR synthetics show that interference of reflected signals leads to reflection patterns that change with frequency. However, the model is too small-scale with respect to both vertical and horizontal resolution of the GPR signal to compare with actual GPR reflections of thinly bedded sediment. Nevertheless, it is important to stress that interfering reflections from laterally continuous thin bedding may cause reflection patterns that do not represent primary bedding. Future studies are needed to improve understanding of thin-layer reflections.

Acknowledgements

This research was partly conducted within the HYDROSED project that combines detailed study of sedimentary structures with in-situ and laboratory measurement of hydraulic properties. We thank DZH (Duinwaterbedrijf Zuid Holland) for permitting fieldwork in their infiltration area and for providing logistical assistance. GPR and TDR equipment was provided by the Faculty of Technical Earth Sciences of Delft University and by the Institute for Biodiversity and Ecosystem Dynamics of the University of Amsterdam. Sytze van Heteren (TNO-NITG) and Jeroen Kenter (VU) were of great help during the fieldwork. We thank Tony Endres (University

of Waterloo) for his suggestions and Marjoke Heneweer (Utrecht University) for comments on an earlier version of the text. We are indebted to Sjef Meekes, Sytze van Heteren, and Ronnie van Overmeeren (TNO-NITG) for discussions. RvD was partly supported by the Netherlands Institute of Applied Geosciences TNO-NITG.

References

- Annan, A. P., Cosway, S. W. & Redman, J. D.** (1991) Water table detection with ground penetrating radar. In: Society Exploration Geophysicists Annual Meeting, Houston, USA. Expanded Abstracts, pp. 494-496.
- Arya, L. M. & Paris, J. F.** (1981) A physioempirical model to predict the soil moisture characteristic from particle-size distribution and bulk density data. *Soil Science Society of America Journal*, 45, 1023-1030.
- Bohl, H. & Roth, K.** (1994) Evaluation of dielectric mixing models to describe the $\theta(\epsilon)$ -relation. In: Time Domain Reflectometry in environmental, infrastructure and mining applications, Bureau of Mines Special Publication, 19, 309-317. US Department of Interior, Evanston.
- Bouma, J.** (1977) Soil survey and the study of water in the unsaturated soil - simplified theory and some case studies. Netherlands Soil Survey Institute, Wageningen, 107 pp.
- Bracco Gartner, G. L.** (2000) High resolution impedance models of outcrops and their applications in seismic interpretation. Ph.D. thesis, Vrije Universiteit Amsterdam, 144 pp.
- Bristow, C. S., Bailey, S. D. & Lancaster, N.** (2000) The sedimentary structure of linear sand dunes. *Nature*, 406(6), 56-59.
- Clement, W. P., Cardimona, S. J., Endres, A. L. & Kadinsky-Cade, K.** (1997) Site characterization at the Groundwater Remediation Field Laboratory. *The Leading Edge*, 16(11), 1617-1621.
- Daniels, D. J., Gunton, D. J. & Scott, H. E.** (1988) Introduction to subsurface radar. *IEE (Institution of Electrical Engineers) Proceedings*, 135(4), 278-320.
- Davis, J. L. & Annan, A. P.** (1989) Ground-penetrating radar for high resolution mapping of soil and rock stratigraphy. *Geophysical Prospecting*, 37, 531-551.
- De Marsily, G.** (1986) Quantitative hydrogeology. Academic Press, London, 440 pp.
- Endres, A. L.** (2000) Size scale considerations in modelling the electrical conductivity of porous rocks and soils. *Exploration Geophysics*, 31, 418-423.

- Fens, T. W.** (2000) Petrophysical properties from small rock samples using image analysis techniques. Ph.D. thesis, Delft University of Technology, 199 pp.
- Gochioco, L. M.** (1992) Modeling studies of interference reflections in thin-layered media bounded by coal seams. *Geophysics*, 57(9), 1209-1216.
- Gupta, S. C. & Larson, W. E.** (1979) Estimating soil water retention characteristics from particle size distribution, organic matter content, and bulk density. *Water Resources Research*, 15, 1633-1635.
- Hänninen, P.** (1992) Application of ground penetrating radar and radio wave moisture probe techniques to peatland investigations. *Geological Survey of Finland Bulletin*, 361, 1-71.
- Haverkamp, R. & Parlange, J. Y.** (1986) Predicting the water-retention curve from particle-size distribution, 1, sandy soils without organic matter. *Soil Science*, 142, 325-339.
- Heimovaara, T. J. & Bouten, W.** (1990) A computer-controlled 36-channel time domain reflectometry system for monitoring soil water contents. *Water Resources Research*, 26(10), 2311-2316.
- Hubbard, S. S., Rubin, Y. & Majer, E.** (1997) Ground-penetrating-radar-assisted saturation and permeability estimation in bimodal systems. *Water Resources Research*, 33(5), 971-990.
- Huggenberger, P.** (1993) Radar facies: recognition of facies patterns and heterogeneities within Pleistocene Rhine gravels, NE Switzerland. In: Braided Rivers (Ed. by J. L. Best & C. S. Bristow), Geological Society Special Publication, 75, 163-176. Geological Society, London.
- Huggenberger, P., Meier, E. & Pugin, A.** (1994) Ground-probing radar as a tool for heterogeneity estimation in gravel deposits: advances in data-processing and facies analysis. *Journal of Applied Geophysics*, 31, 171-184.
- Jelgersma, S., De Jong, J., Zagwijn, W. H. & Van Regteren Altena, J. F.** (1970) The coastal dunes of the western Netherlands; geology, vegetational history and archeology. *Mededelingen Rijks Geologische Dienst*, Nieuwe Serie 21, 93-167.
- Kallweit, R. S. & Wood, L. C.** (1982) The limits of resolution of zero-phase wavelets. *Geophysics*, 47(7), 1035-1046.

- Knapp, R. W.** (1990) Vertical resolution of thick beds, thin beds, and thin-bed cyclothem. *Geophysics*, 55(9), 1183-1190.
- Knoll, M. D. & Knight, R.** (1994) Relationships between dielectric and hydrogeologic properties of sand-clay mixtures. In: 5th International Conference on Ground Penetrating Radar, Waterloo Centre for Groundwater Research, Canada. pp. 45-61.
- Kowalsky, M. B., Dietrich, P., Teutsch, G. & Rubin, Y.** (2001) Forward modeling of ground-penetrating radar data using digitized outcrop images and multiple scenarios of water saturation. *Water Resources Research*, 37(6), 1615-1625.
- Kruse, S. E. & Jol, H. M.** (submitted) Amplitude and waveform analysis of repetitive GPR reflections: Lake Bonneville Delta, Utah. In: Ground penetrating radar in sediments: applications and interpretation (Ed. by C. S. Bristow & H. M. Jol), Geological Society Special Publication. Geological Society, London.
- Mayer, L. A.** (1979) Deep sea carbonates: acoustic, physical and stratigraphic properties. *Journal of Sedimentary Petrology*, 49(3), 819-836.
- Mayer, L. A.** (1980) Deep-sea carbonates: physical property relationships and the origin of high-frequency acoustic reflectors. *Marine Geology*, 38, 165-183.
- Mishra, S., Parker, J. C. & Singhal, N.** (1989) Estimation of soil hydraulic properties and their uncertainty from particle size distribution data. *Journal of Hydrology*, 108, 1-18.
- Roksandic, M. M.** (1995) Discussion on 'A 3-D seismic case history evaluating fluvially deposited thin-bed reservoirs in a gas-producing property', by B. A. Hardage, R. A. Levy, V. Pendleton, J. Simmons, & R. Edsen with reply by the authors. *Geophysics*, 60(5), 1585-1592.
- Roth, K., Schulin, R., Flühler, H. & Attinger, W.** (1990) Calibration of time domain reflectometry for water content measurement using a composite dielectric approach. *Water Resources Research*, 26(10), 2267-2273.
- Saarenketo, T.** (1998) Electrical properties of water in clay and silty soils. *Journal of Applied Geophysics*, 40, 73-88.

- Saxton, K. E., Rawls, W. J., Romberger, J. S. & Papendick, R. I.** (1986) Estimating generalized soil water characteristics from texture. *Soil Science Society of America Journal*, 50(4), 1031-1036.
- Schaap, M. G.** (1996) The role of soil organic matter in the hydrology of forests on dry sandy soils. Ph.D. thesis, University of Amsterdam, 145 pp.
- Schaap, M. G. & Bouten, W.** (1996) Modeling water retention curves of sandy soils using neural networks. *Water Resources Research*, 32(10), 3033-3040.
- Sensors&Software** (1996) pulseEKKO synthetic radargram user's guide, Sensors&Software, Mississauga, 18 pp.
- Sutinen, R.** (1992) Glacial deposits, their electrical properties and surveying by image interpretation and ground penetrating radar. *Geological Survey of Finland Bulletin*, 359, 1-123.
- Topp, G. C., Davis, J. L. & Annan, A. P.** (1980) Electromagnetic determination of soil water content: measurements in coaxial transmission lines. *Water Resources Research*, 16(3), 574-582.
- Topp, G. C. & Davis, J. L.** (1985) Measurement of soil water content using time-domain reflectometry (TDR): a field evaluation. *Soil Science Society of America Journal*, 49, 19-24.
- Van Dam, R. L.** (2001) Causes of ground-penetrating radar reflections in sediment. Ph.D. thesis, Vrije Universiteit Amsterdam, 110 pp.
- Van Dam, R. L. & Schlager, W.** (2000) Identifying causes of ground-penetrating radar reflections using time-domain reflectometry and sedimentological analyses. *Sedimentology*, 47(2), 435-449.
- Van Dam, R. L., Schlager, W., Dekkers, M. J., & Huisman, J. A.** (accepted1). Iron oxides as a cause of GPR reflections. *Geophysics*, scheduled for publication in the March/April 2002 issue, 67(2).

- Van Dam, R. L., Van Den Berg, E. H., Van Heteren, S., Kasse, C., Kenter, J. A. M., & Groen, K.** (accepted2). Influence of organic matter in soils on radar-wave reflection: sedimentological implications. *Journal of Sedimentary Research*, scheduled for publication in the May 2002 issue, 72(3).
- Van Den Berg, E. H., Meesters, A. G. C. A., Kenter, J. A. M. & Schlager, W.** (in press) Automated separation of touching grain sections in digital images. *Computers and Geosciences*, scheduled for publication in the February 2002 issue, 28(1).
- Van Den Berg, E. H., Bense, V. F. & Schlager, W.** (in review) Textural characteristics and fabric in laminated sand with digital image analysis of thin sections. *Journal of Sedimentary Research*.
- Van Der Kruk, J.** (2001) Three-dimensional imaging of multi-component ground penetrating radar data. Ph.D. thesis, Delft University of Technology, 242 pp.
- Van Genuchten, M. T.** (1980) A closed-form equation for predicting the hydraulic conductivity of unsaturated soils. *Soil Science Society of America Journal*, 44, 892-898.
- Vogel, H. J.** (2000) A numerical experiment on pore size, pore connectivity, water retention, permeability and solute transport using network models. *European Journal of Soil Science*, 51, 99-105.
- Vogel, H. J. & Roth, K.** (1998) A new approach for determining effective soil hydraulic functions. *European Journal of Soil Science*, 49, 547-556.
- Young, R. A. & Sun, J.** (1999) Revealing stratigraphy in ground-penetrating radar data using domain filtering. *Geophysics*, 64(2), 435-442.

Table 1: Details of GPR sections and common-mid-point measurements (Locations in Figure 1).

Name	X_0, Y_0 [m]	X_{max}, Y_{max} [m]	f [MHz]	Step size [m]
1	0.00, 0.00	15.75, 0.00	450	0.050
1	6.00, 0.00	10.00, 0.00	900	0.025
5	6.00, 0.75	10.00, 0.75	900	0.025
6	0.00, 1.50	16.00, 1.50	450	0.050
6	6.00, 1.50	10.00, 1.50	900	0.025
7	6.00, 2.25	10.00, 2.25	900	0.025
2	0.00, 3.00	15.90, 3.00	450	0.050
2	6.00, 3.00	10.00, 3.00	900	0.025
G	6.00, 0.00	6.00, 3.00	450	0.050
G	6.00, 0.00	6.00, 3.00	900	0.025
C	8.00, 0.00	8.00, 10.95	450	0.050
C	8.00, 0.00	8.00, 3.00	900	0.025
H	10.00, 0.00	10.00, 3.00	450	0.050
H	10.00, 0.00	10.00, 3.00	900	0.025
CMP 1	6.00, 0.00	-	450	0.050
CMP 4	8.00, 1.50	-	900	0.020

$f = \text{frequency}$.

Table 2: Textural characteristics of the samples from unit 7 in trench I. Clay and silt are defined as the weight fractions smaller than $2\ \mu\text{m}$ and between 2 and $62\ \mu\text{m}$, respectively. The two most relevant core plugs are shown in Figure 2.

	N	Grain size [μm]		Clay content		Silt content		Organic matter	
		Mean	Sd	%	Sd	%	Sd	%	Sd
Vertical transect	15	280.13	25.73	0.43	0.05	0.61	0.11	0.46	0.21
Core plugs	19	268.79	12.08	0.57	0.05	1.07	0.13	0.10	0.16

N = number of samples; Sd = standard deviation.

Table 3: Textural characteristics of the samples from unit 7 in trench I. Clay and silt are defined as the weight fractions smaller than $2\ \mu\text{m}$ and between 2 and $62\ \mu\text{m}$, respectively. The two most relevant core plugs are shown in Figure 2.

Sample	N	Grain size [μm]		η [m^3m^{-3}]
		Mean	Sd	
20	321	303.325	144.373	0.376
27	387	285.545	104.758	0.325
61	615	209.996	64.805	0.335
69	553	223.066	69.790	0.377
Average for 1-85	492	245.852	89.752	0.358
<i>I21p</i>	-	293.209	85.879	0.446

N = number of samples; *Sd* = standard deviation;

η = porosity.

Table 4: Neural network input and output for 4 specific samples in thin section I21 and for the average of all 85 samples. Values for input parameters gravel percentage and organic-matter percentage were set to zero whereas θ_s input was set equal to porosity (Table 3) and dry bulk density was calculated through $\rho_b = 2.65(1 - \eta)$. Output parameters α_{vg} and n define the position of the inflection point and the amount of curvature in the θ - pF relationship (Equation (1)), respectively. The marginal difference between porosity (Table 3) and modeled saturated water content output can be neglected. Laboratory measurement results for core plug I21p are given for comparison (in italics).

Sample	Model input			Model output		
	d_{gsd} [μm]	n_{gsd}	ρ_b [g cm^{-3}]	α_{vg} [cm^{-1}]	n	θ_s [m^3m^{-3}]
20	346.856	4.080	1.654	0.032	2.614	0.379
27	311.210	5.533	1.789	0.027	2.871	0.326
61	224.326	6.841	1.762	0.019	3.512	0.336
69	238.855	6.819	1.651	0.024	3.576	0.379
Average for 1-85	266.531	5.529	1.700	0.025	3.153	0.360
<i>I21p</i>	-	-	<i>1.467</i>	<i>0.024</i>	<i>6.99</i>	<i>0.446</i>

d_{gsd} = measure for average grain size; n_{gsd} = GSD uniformity; ρ_b = dry bulk density; θ_s = saturated water content.

Table 5: Volumetric water content (θ) and relative permittivity (ϵ_r) at pF 2, for 4 specific samples in thin section I21, for the average of all 85 samples and for core plug I21p (in italics). For the thin section samples θ was estimated using the neural network (Table 4). For the core plug the water-retention characteristics were measured in the lab and fitted with Equation (1) to find θ at pF 2. Relative permittivity was calculated from Equation (3). The θ and ϵ_r values for the core plug are low compared to the thin-section samples. The steep plateaus in the water-retention curves partly cause the large difference because θ is very sensitive to small variations in the height of the plateau.

Sample	θ [m^3m^{-3}]	ϵ_r
20	0.056	4.09
27	0.048	4.02
61	0.059	4.33
69	0.039	3.56
Average for 1-85	0.052	4.03
<i>I21p</i>	<i>0.010</i>	<i>2.53</i>

θ = volumetric water content;

ϵ_r = relative permittivity.

Figure 1: (a) Study site with trenches. The inset shows the location of the study area in The Netherlands. The dashed lines mark the detailed survey area, imaged with 450- and 900-MHz antennas. (b) Measurement grid.

Figure 2: (a) Trench wall panorama showing sedimentary units and (b) lacquer peels of the trench. The lacquer peels show faint foreset lamination indicated by thin dashed lines and the locations of grain-size samples (vertical spacing 0.05 m), TDR measurements, box cores, and core plugs.

Figure 3: GPR sections from line 1 that allow correlation with the trench wall panoramas and lacquer peels in Figure 2. The 450-MHz image (a) has the same horizontal and vertical scale as Figure 2a. In the 900-MHz image (b), which has a horizontal and vertical scale half that of Figure 2b, the frame shows the outline of the lacquer peels in Figure 2b. The numbered labels in the radar sections refer to the text and represent: ①, reflection from the top of unit 6; ②, reflection from unit 2 and 4; ③, reflection from foreset associated with sample I21 in Figure 2b; ④, reflection from foreset associated with sample I22 in Figure 2b. Both radar sections are plotted with an AGC gain.

Figure 4: Variation in relative permittivity (ϵ_r) for TDR sections (a) 1223.002 and (b) 1223.001 with depth and (c) variation in grain size with depth (see Figure 2 for locations). The numbered labels ③ and ④ correspond approximately to the clinofolds indicated in Figure 3. The fact that event ③ in TDR section 1223.002 and event ④ in TDR section 1223.001 have about the same depth is the result of the dipping of the foresets. In the grain-size section, the fine grain sizes associated with the foreset tops in Figure 2 are superimposed on the large-scale trend in grain size.

Figure 5: Four cross plots illustrating the influence of sedimentary structures on relative permittivity. TDR sections 1223.005, 1223.006, and 1223.007 were measured at locations of known foreset tops; section 1223.008 was taken at a position where no foreset was visible. See Figure 2 for the locations. The numbered labels ③ and ④ correspond to those in Figures 3 and 4.

Figure 6: Digitized thin section of box core I21. The image is based on four high-resolution (176×176 pixels per mm^2) overlapping photographs that were taken perpendicular to the sedimentary structures under an angle with the vertical (Figure 2b). Here, the image is tilted towards vertical such that the sedimentary layering appears approximately horizontal. The ruler to the right of the image shows the positions of the 85 samples. For sample 1 the measurement window is shown. Marked samples 20, 27, 61, and 69 have characteristic texture (Figure 7a,b) and are analyzed in Figure 9.

Figure 7: Vertical transects of (a) mean grain size and (b) porosity along the long axis of thin section I21. (c) The water-content at pF 2 along the same transect was calculated using a neural network model that describes the θ - pF relationship based on cumulative grain-size distribution and porosity. (d) The relative permittivity was calculated using a dielectric mixing model (Equation (3)). Open circles indicate specific samples 20, 27, 61, and 69 that are analyzed in Figure 9.

Figure 8: Cross plot of porosity versus mean grain size for thin section I21.

Figure 9: Plots of (a) cumulative grain-size distribution (GSD) and (b) water-retention characteristics for samples 20, 27, 61, and 69 in thin section I21 and for core plug I21p. The 4 specific samples in thin section I21 are characteristic in mean grain size (Figure 7a) and porosity (Figure 7b). The positions are shown in Figure 6. The cumulative GSD's from the thin section were calculated using Van Den Berg et al. (in review) and fitted with Equation (2). The grain size from the core-plug sediment (location in Figure 2a) was measured with a laser-particle sizer. The θ - pF relation was calculated using a neural network model (Schaap and Bouten, 1996) for the thin section samples and using standard lab measurement techniques for the core plug. The open circles represent the lab data for I21p; the solid line is the fit with Equation (1).

Figure 10: Radar reflectivity and synthetic radar traces constructed from (a) TDR measurements 1223.005 and 1223.006 in Figure 5 and (b) the image analysis results in Figure 7d. The impedance models used for the synthetic modeling assume a 0.2-m thick homogeneous layer before the first event. The impedance and *RC* models have a depth scale whereas the synthetic traces have a time scale. Since wave velocity varies with depth, relative thickness of the layers changes. The synthetic radar traces have the same horizontal scale. The dashed wiggle shows the wavelet that was used to convolve with the impulse response model. The numbered arrows ① - ④ are referred to in the text.

Figure 11: Diagrams showing the stack of 6 interfering reflections from the TDR-based impedance model at (a) 900 MHz and (b) 450 MHz. The numbers 1 to 6 refer to the events in the TDR reflectivity model (Figure 10a). The composite trace is dominated by destructive and constructive interference. We ignored multiples and interlayer reflections as we consider them to contribute little to the total reflection.

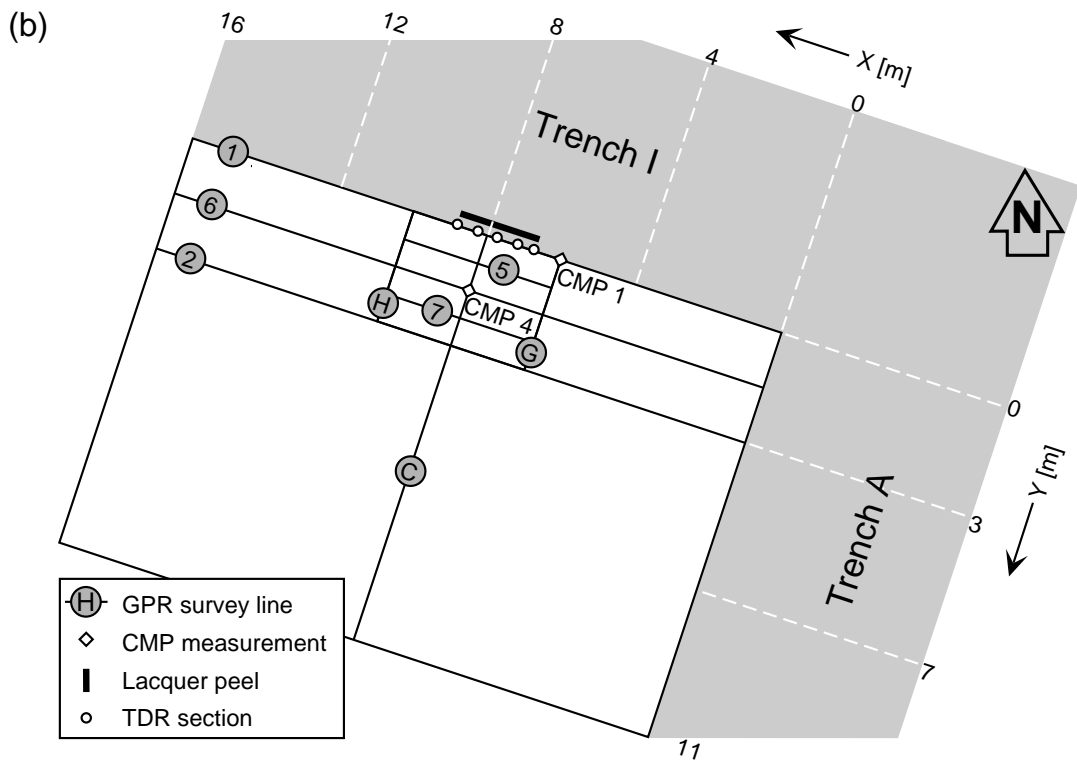
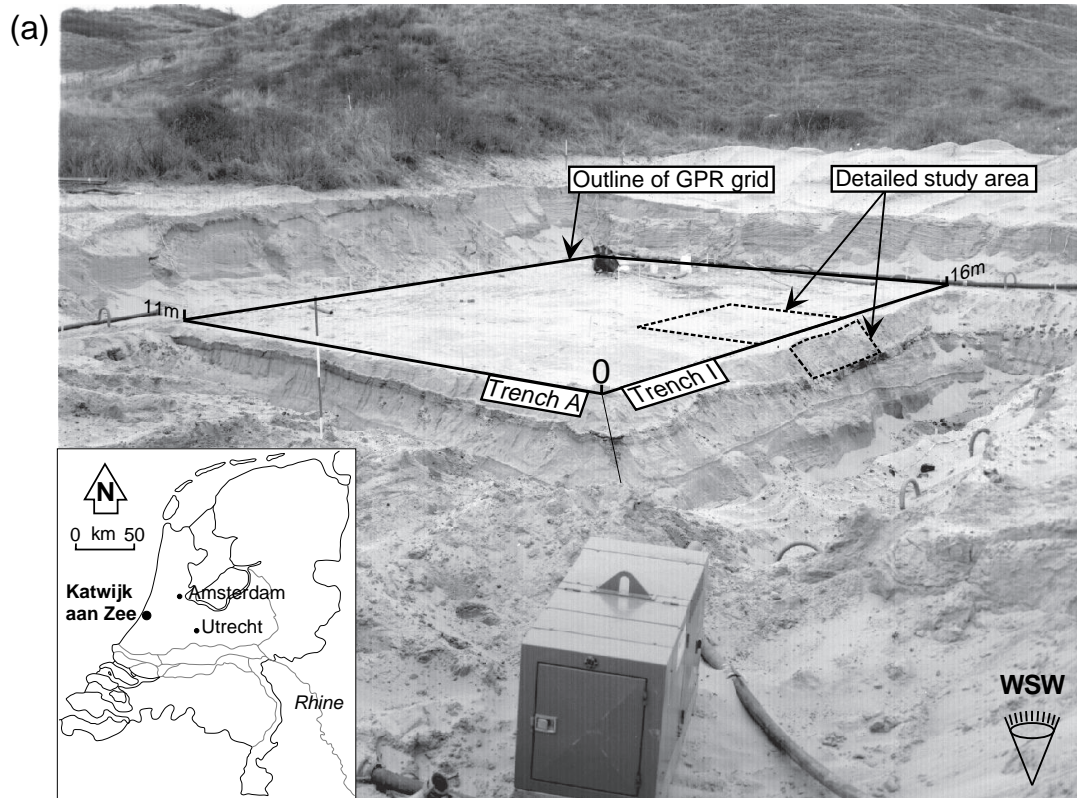


Figure 1

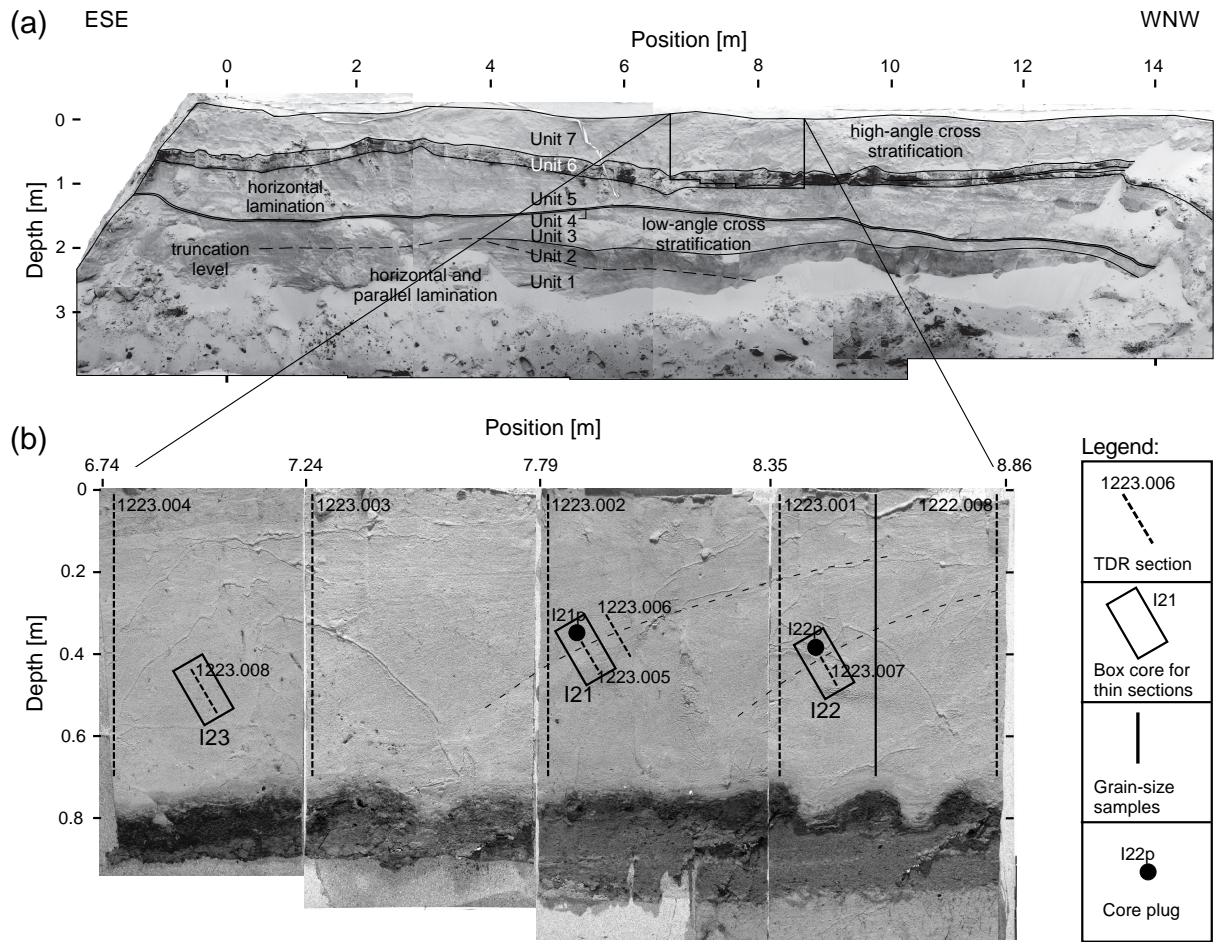


Figure 2

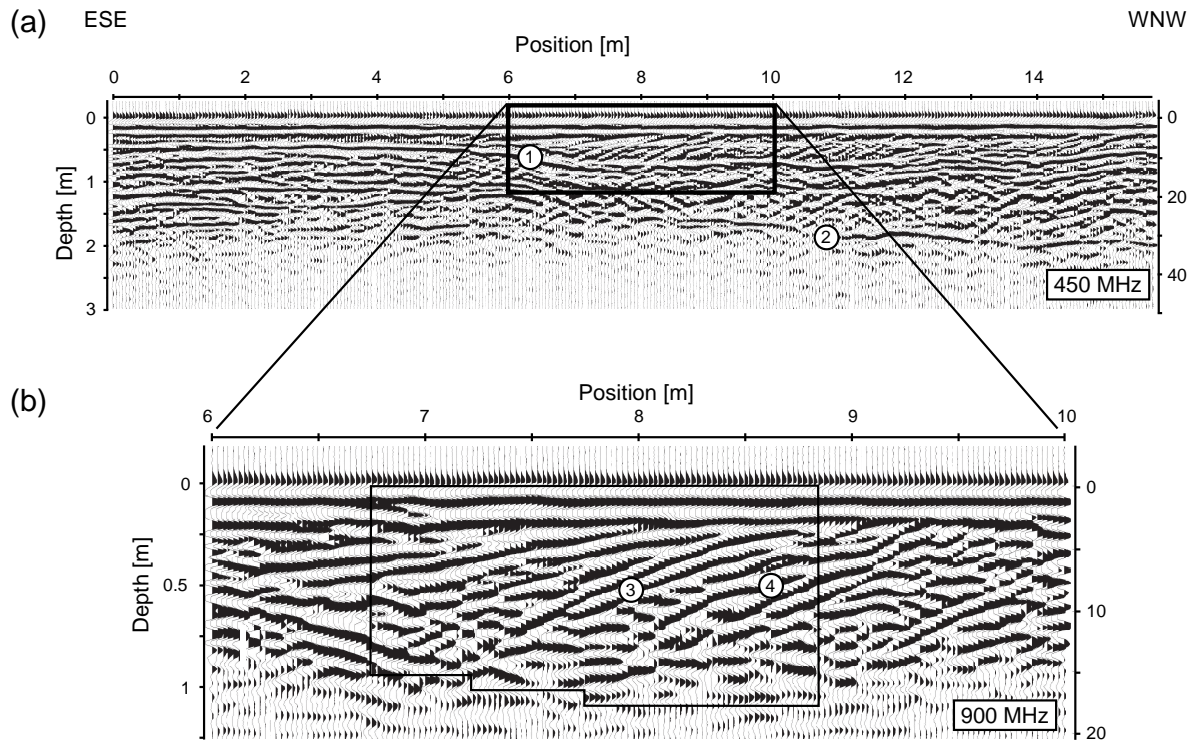


Figure 3

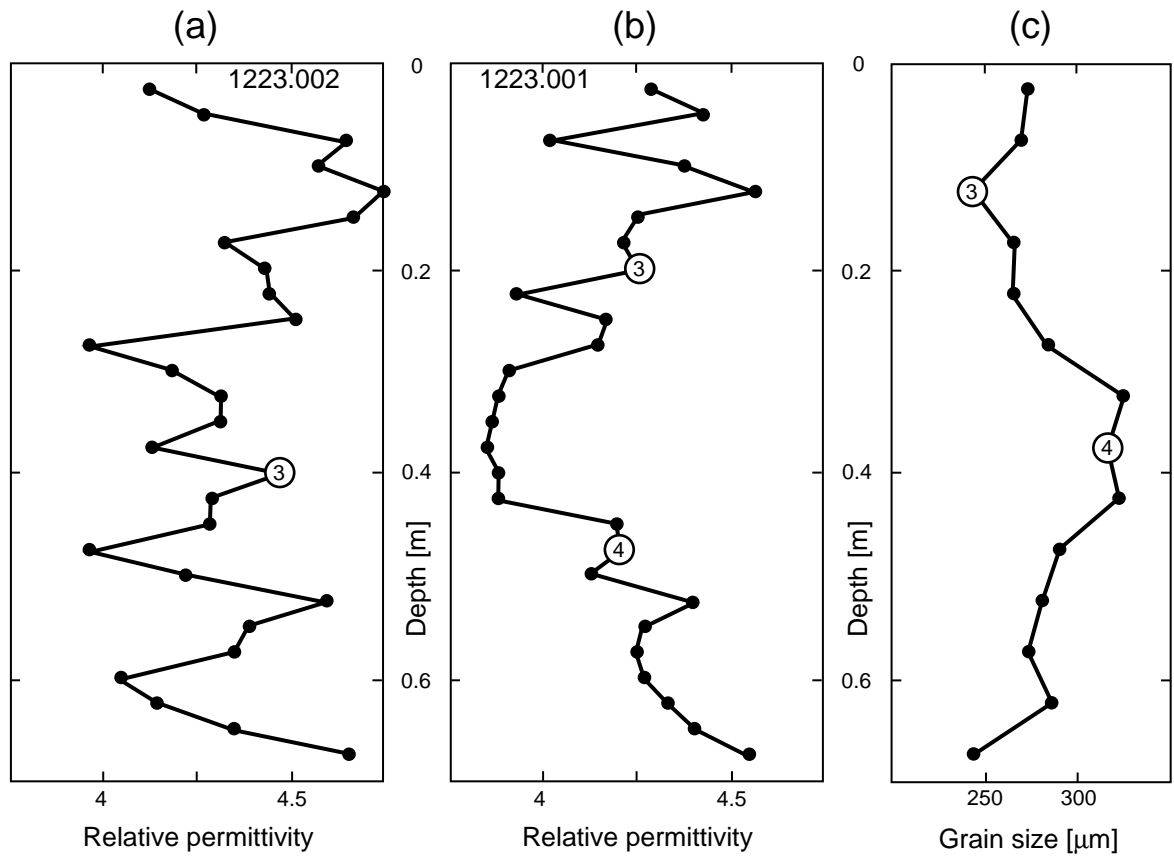


Figure 4

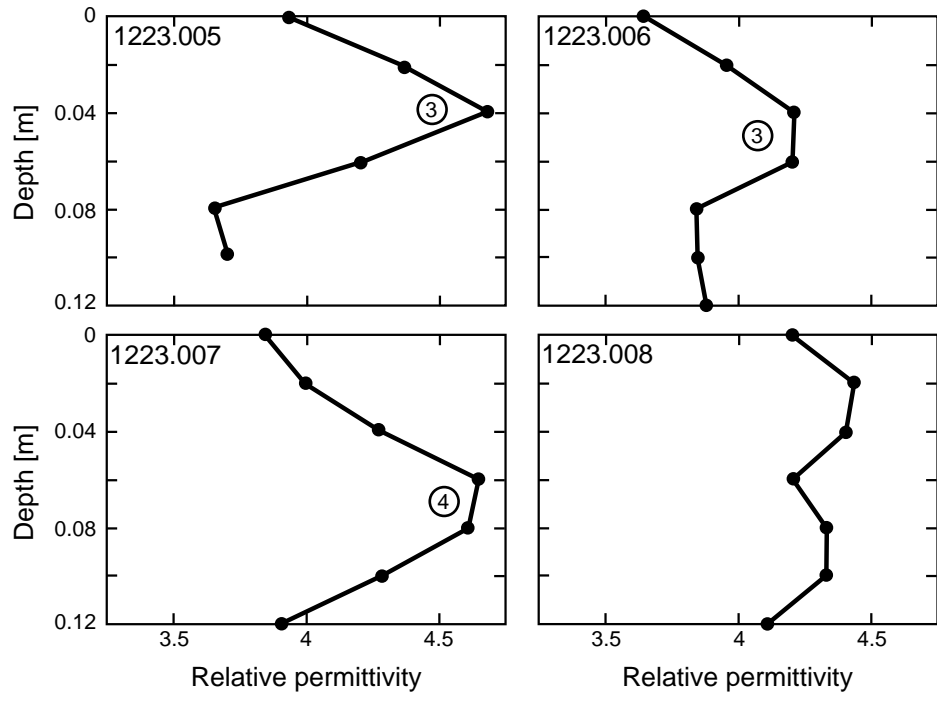


Figure 5

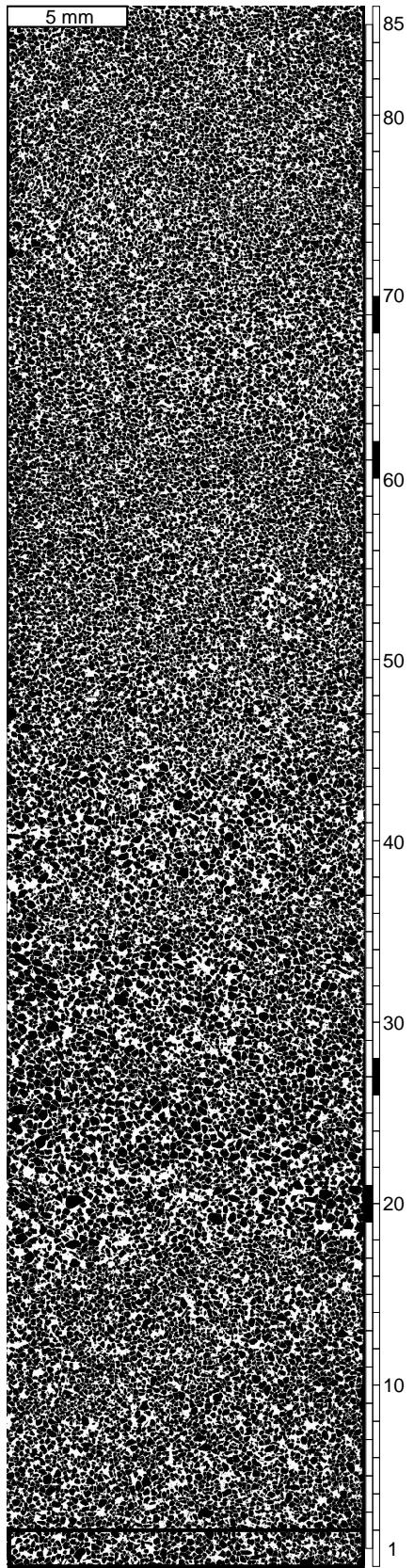


Figure 6

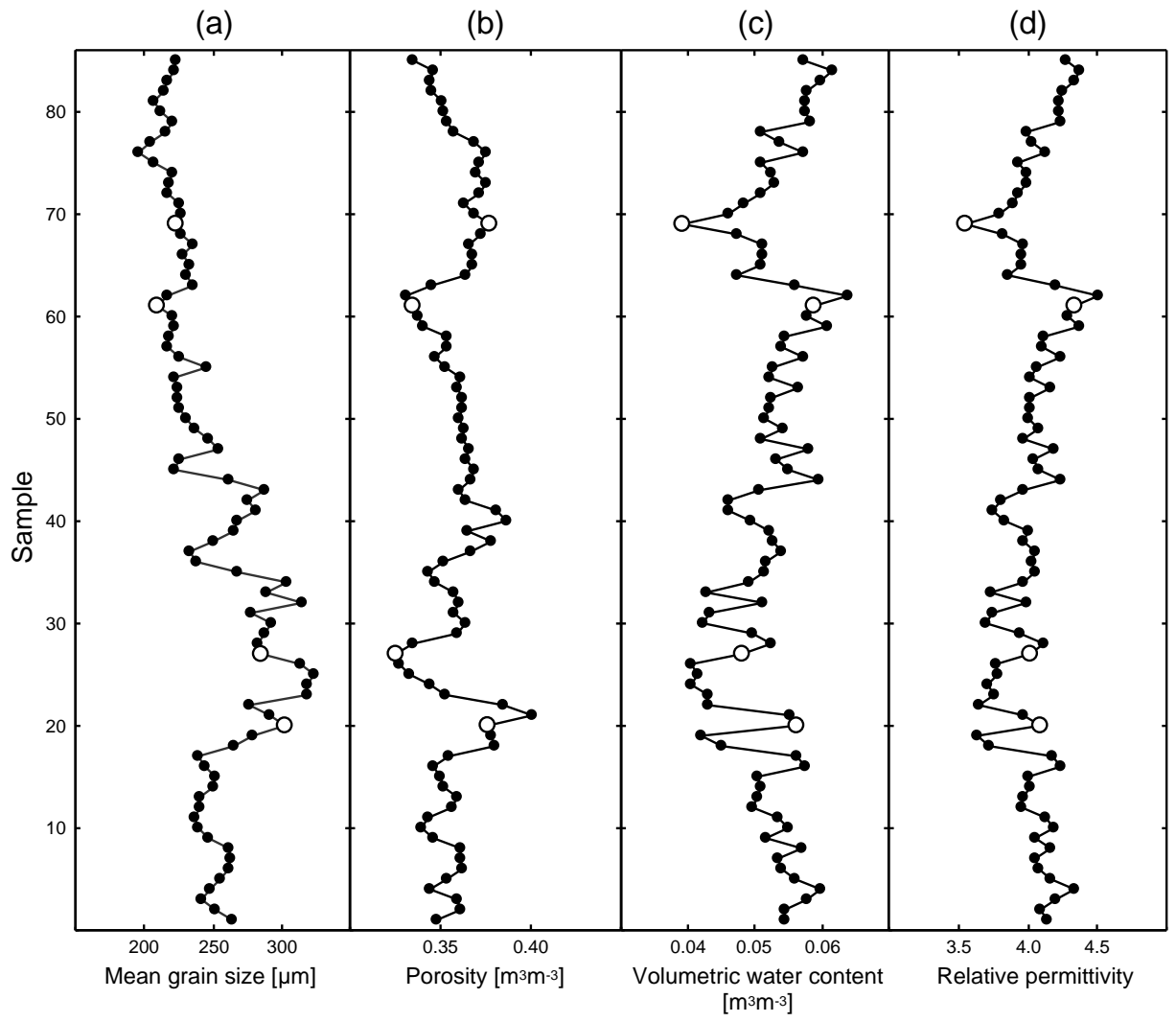


Figure 7

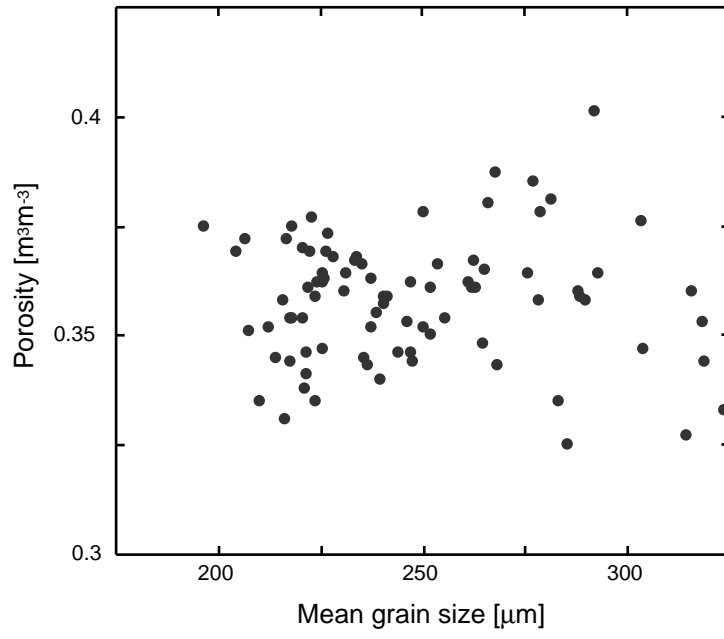


Figure 8

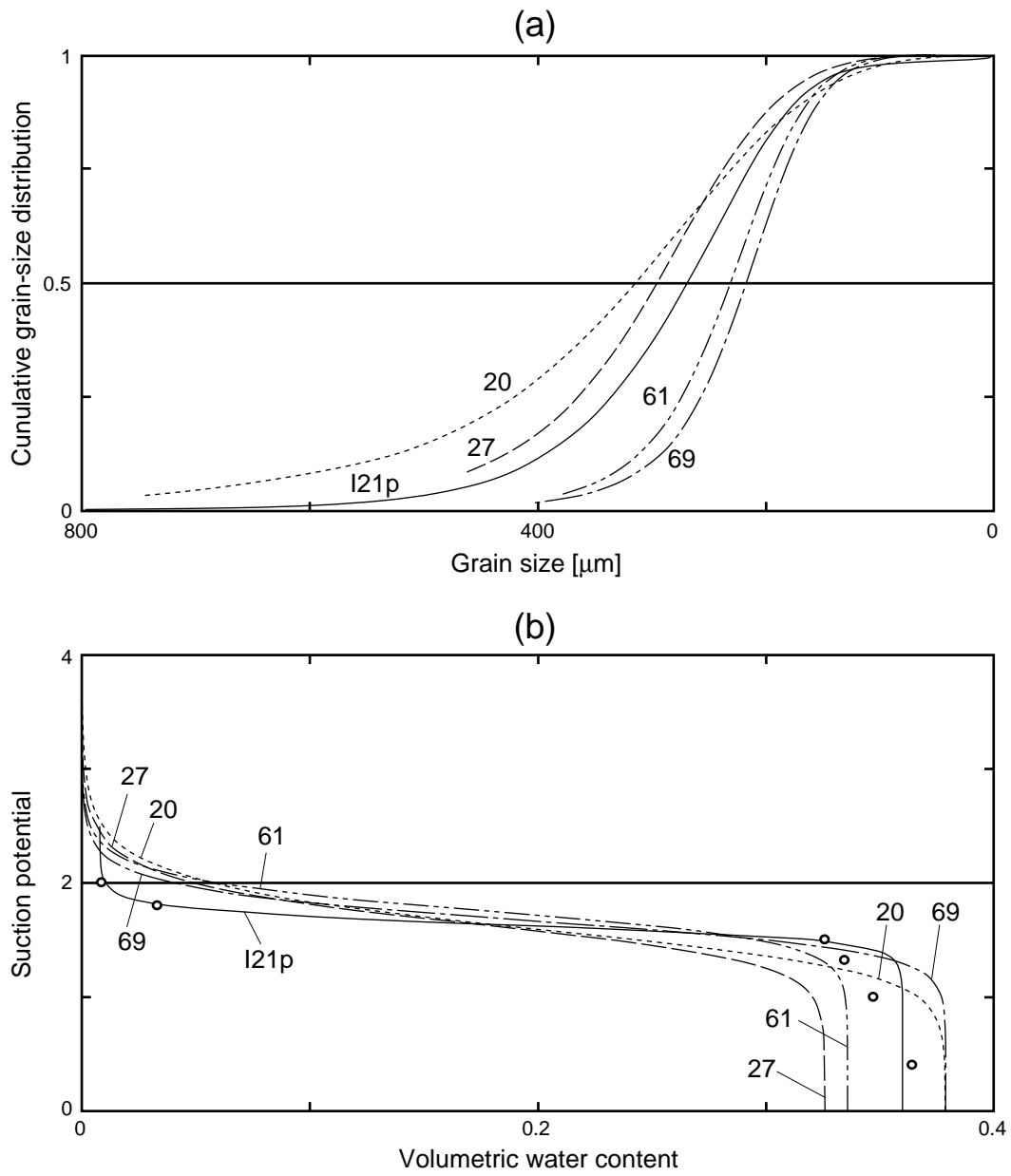


Figure 9

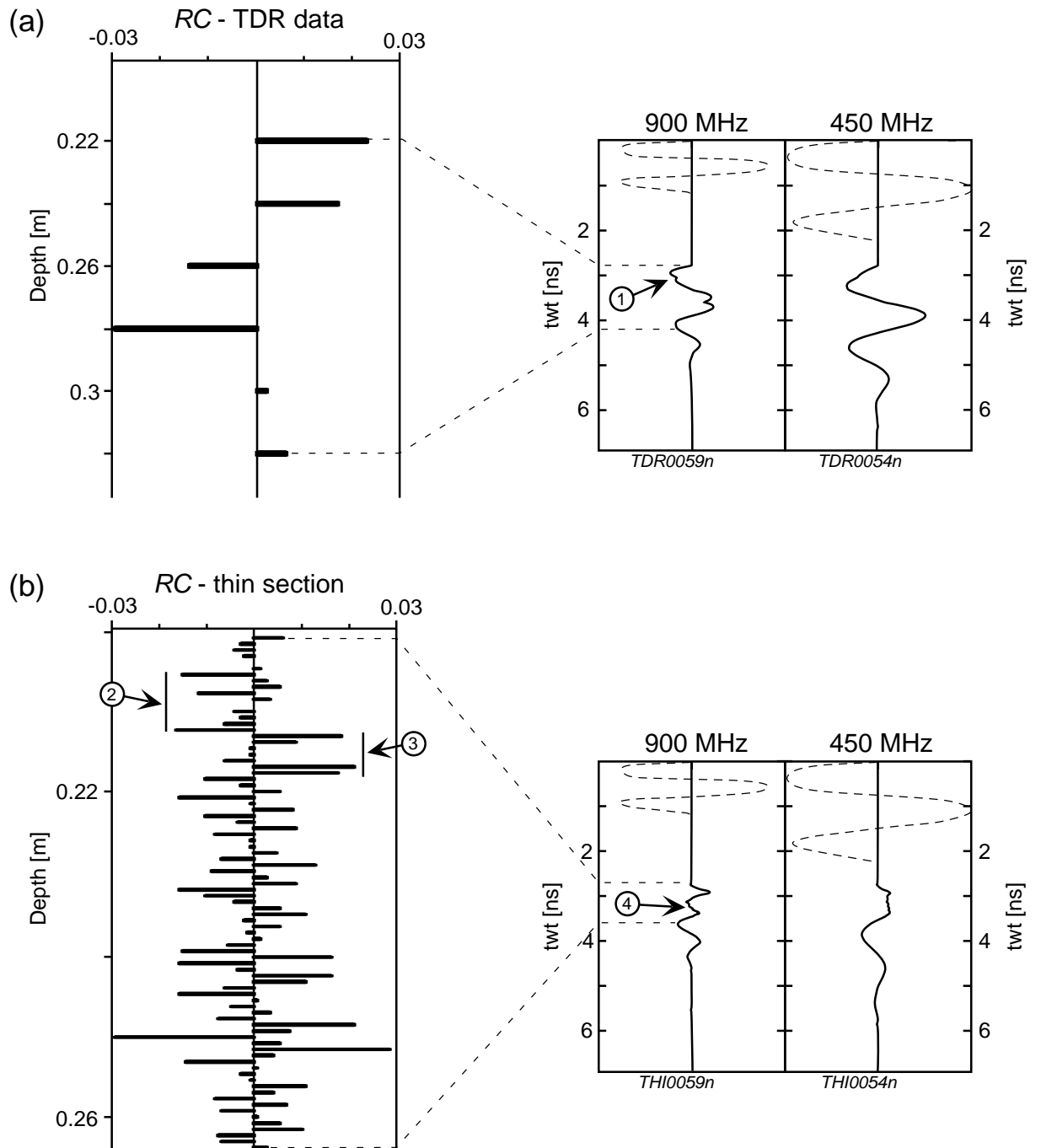


Figure 10

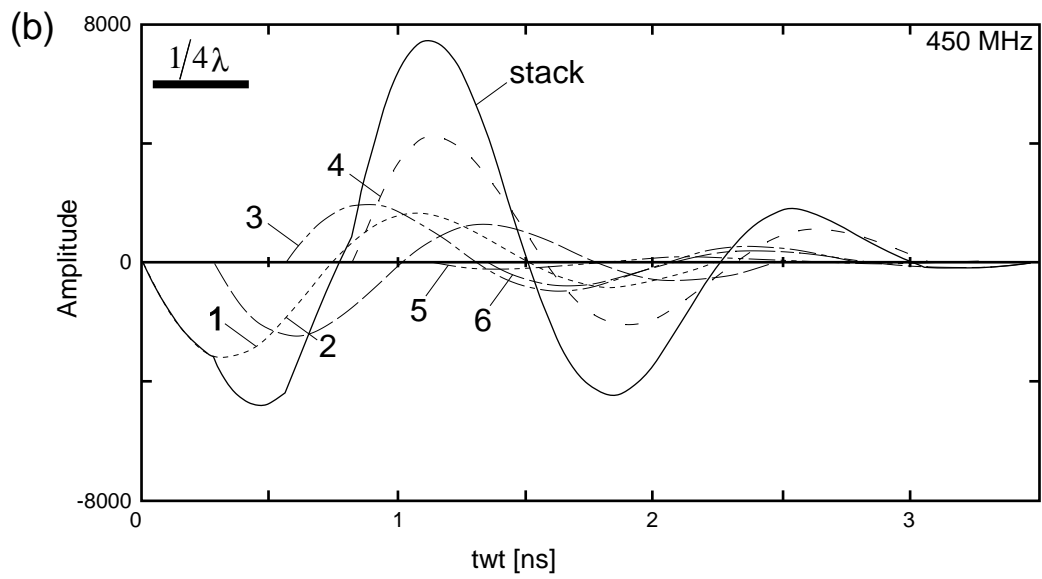
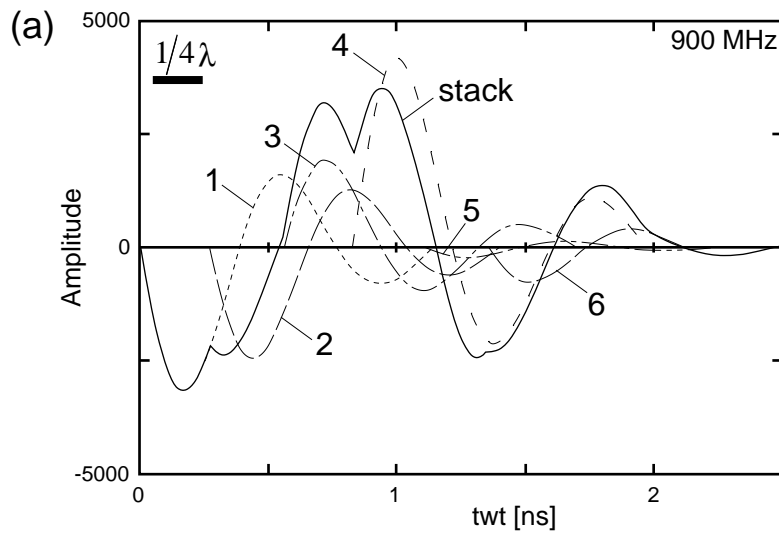


Figure 11